

Vanadium Dioxide-Based Miniaturized Thermal Sensors: Humidity Effects on Phase Change and Sensitivity

Peter Francis Mathew Elango,* Sumaiya Kabir, Ponnappa Kechanda Prasanna, Mei Xian Low, Mingjie Yang, Sudip Chakraborty, Sumeet Walia, Sharath Sriram, and Madhu Bhaskaran*



Cite This: *ACS Appl. Electron. Mater.* 2022, 4, 5456–5467



Read Online

ACCESS |

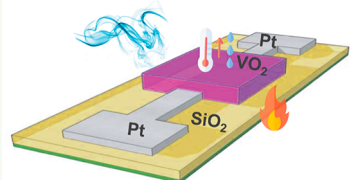
Metrics & More

Article Recommendations

Supporting Information

ABSTRACT: With rapid advancements in technology in the electronics sector, demand for the miniaturization of devices while retaining their functionality is on the rise. Metal oxide-based thermal sensors are desired, owing to their enhanced sensing capabilities and low cost of operation. Highly sensitive metal oxide sensors can enable stable, accurate, and miniaturized thermal sensors tailored to different operational ranges. However, the influence of humidity and how it affects the sensitivity of the material by interacting with the material surface has not been extensively studied. In this work, we report a vanadium dioxide (VO_2)-based thin film thermal sensor studied under the influence of varying humidity conditions. The effect of different humidity levels on the overall thermal sensing behavior and the insulator-to-metal transition (IMT) phenomenon was investigated. Further, density functional theory (DFT) studies were conducted to understand the thermal sensing mechanism under changing humidity conditions. The developed sensor exhibited a good response over a broad temperature range of -100 to 100 °C, with a TCR of -0.00243% , high sensitivity, and cyclic repeatability. Wireless measurement capabilities were also demonstrated. Such sensors could potentially be used in environmental sensing applications.

KEYWORDS: vanadium dioxide, microthermal sensors, environmental sensors, humidity, surface-mountable sensors



INTRODUCTION

In recent years, environmental sensing has become an increasingly important area of research. Temperature is one of the vital physical parameters in environmental monitoring. Though conventional metal-based temperature sensors offer a higher sensing range and stable operation, they often suffer from low resolution.¹ Metal oxide-based thermal sensors have drawn much attention due to their higher temperature coefficient of resistance (TCR) property, which helps improve performance and resolution. Metal oxide-based thermal sensors fall under the category of thermistors. They exhibit two different types of response: positive temperature coefficient of resistance (PTC) and negative temperature coefficient of resistance (NTC). Commonly employed NTC thermistors are made from oxides of nickel,^{2–7} cobalt,⁸ manganese,^{4,5,8} and iron.^{9,10} Other oxides used to make NTC thermistors include zinc oxide^{6,11} and copper oxide.^{10,12} PTC thermistors are typically made from oxides of barium¹³ and strontium titanate.¹⁴ Temperature sensors with a wide range of temperature measurements under different humidity conditions are desirable. This has led to an investigation on alternative oxides required for low–high temperature range applications such as in space stations,¹⁵ greenhouses,¹⁶ blood cold chain,¹⁷ mining,¹⁸ and medical applications.¹⁹

Vanadium dioxide (VO_2) is an NTC material that has been shown to have a steady response to temperature changes,^{20–24} making it an attractive candidate for temperature sensors. However, the sensing range of the already reported VO_2

sensors is narrow, as shown in Table 1. Furthermore, there is limited understanding of the influence of humidity on the thermal sensing performance, which is crucial for the practical application of these sensors, particularly in environmental temperature monitoring. VO_2 undergoes an insulator-to-metal transition (IMT) at around 68 °C.²⁵ During IMT, the resistivity of VO_2 changes by an order of 10^3 – 10^5 from a high resistance (HR) state in the insulator (M1) phase region to a low resistance (LR) state in the metallic (R) phase region. The effect of varying humidity levels on this exotic IMT property of VO_2 has also not been investigated so far.

We have reported in this work the effects of varying humidity levels on the overall thermal sensing behavior of the developed VO_2 devices and the effect of humidity levels on the IMT properties of the material. Further, the dynamic thermal sensing behavior of the device was investigated over a broad temperature range from -100 to 100 °C. Our developed VO_2 thermal sensor was found to have significantly better performance in comparison with previously reported work, with a broad range of operation, a TCR of -0.00243% , cyclic stability, and high sensitivity, as presented in Table 1. Further,

Received: August 23, 2022

Accepted: October 30, 2022

Published: November 10, 2022

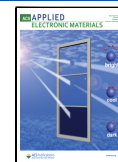


Table 1. Comparison of This Work with Previously Reported VO₂-Based Thermal Sensors

Material	Deposition method	Temperature range	TCR (%)	Studied under influence of humidity?	Reference
VO ₂ thin film	DC sputtering	−100 to 100 °C	−0.00243% [−100 to 62 °C]	Yes	This work
VO ₂ nanoribbons	Analytical proposal	30–85 °C		No	M. A. Baqir et al. ²⁰
VO ₂ thin film	Sol-gel method, Ar ⁺ process	20–80 °C		No	Kim et al. ²¹
VO ₂ thin film	Polymer assisted deposition	−3.15 to 46.45 °C	−0.0112%	No	Liao et al. ²²
VO ₂ -based composite	DC spray	20–80 °C		No	L. H. C. de Lima Junior et al. ²³
VO ₂ (3-fl)–CNT composite	Drop casting	25–80 °C	−(0.9–1.3)% at DC voltage −(1.1–1.3)% at AC voltage	No	K. S. Karimov et al. ²⁴

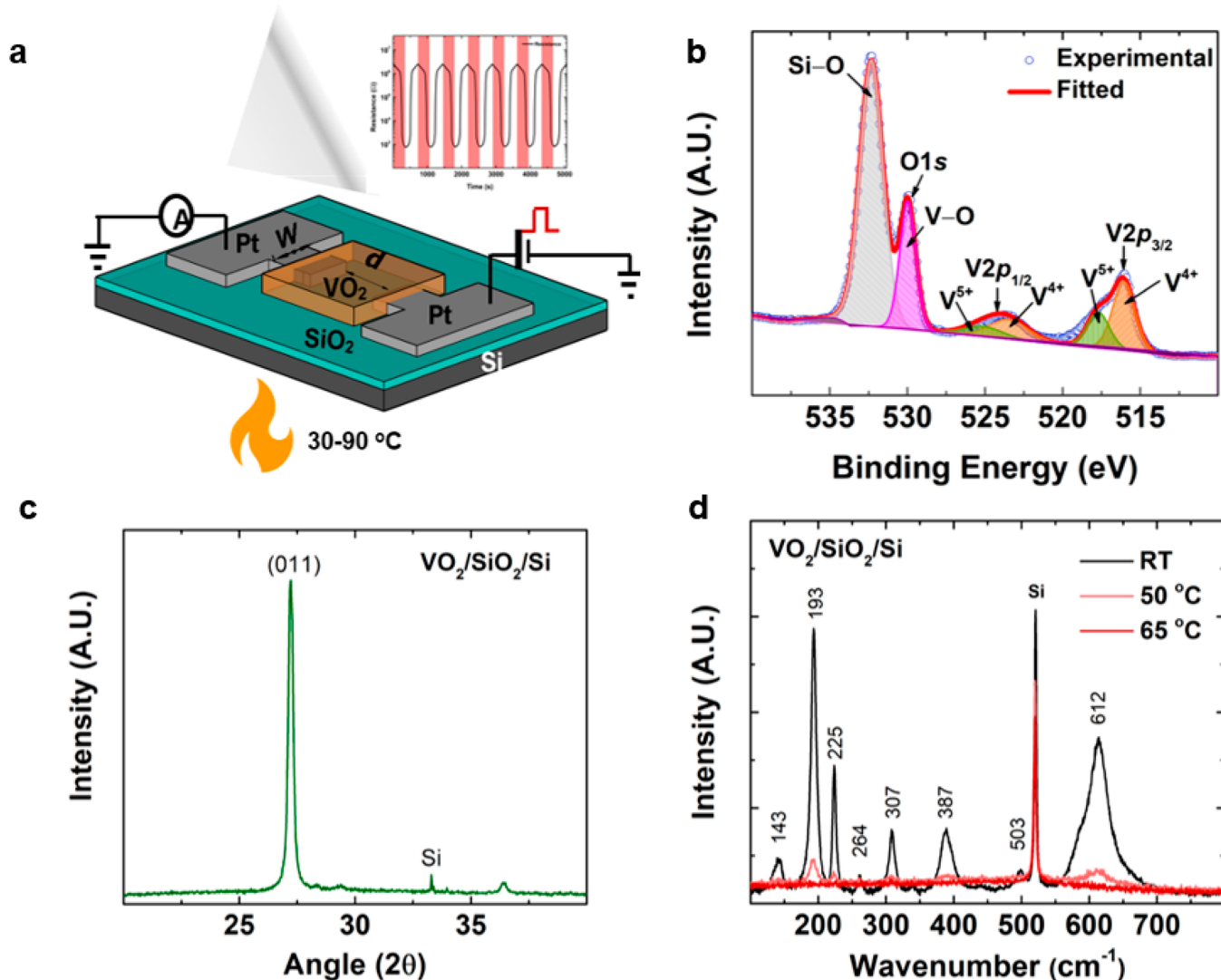


Figure 1. Device schematic and material characterizations of VO₂ thin film devices. (a) Device schematic showing the experimental setup, temperature input, and resistance output during heating and cooling. (b) X-ray photoelectron spectroscopy of crystalline VO₂ thin films showing V⁴⁺ dominance. (c) X-ray diffractogram of crystalline VO₂ thin films deposited on SiO₂/Si, confirming the M1 phase. (d) Temperature-dependent Raman spectra showing VO₂ (M1) peaks and reduction of peak intensity with temperature, confirming insulator-to-metal transition in VO₂.

density functional theory (DFT) computational studies have been presented to provide insights into the working mechanism of the developed VO₂ sensor and its interaction

with water molecules under different humidity conditions. Finally, interfacing with Bluetooth-based wireless sensing capability has been shown to demonstrate potential in

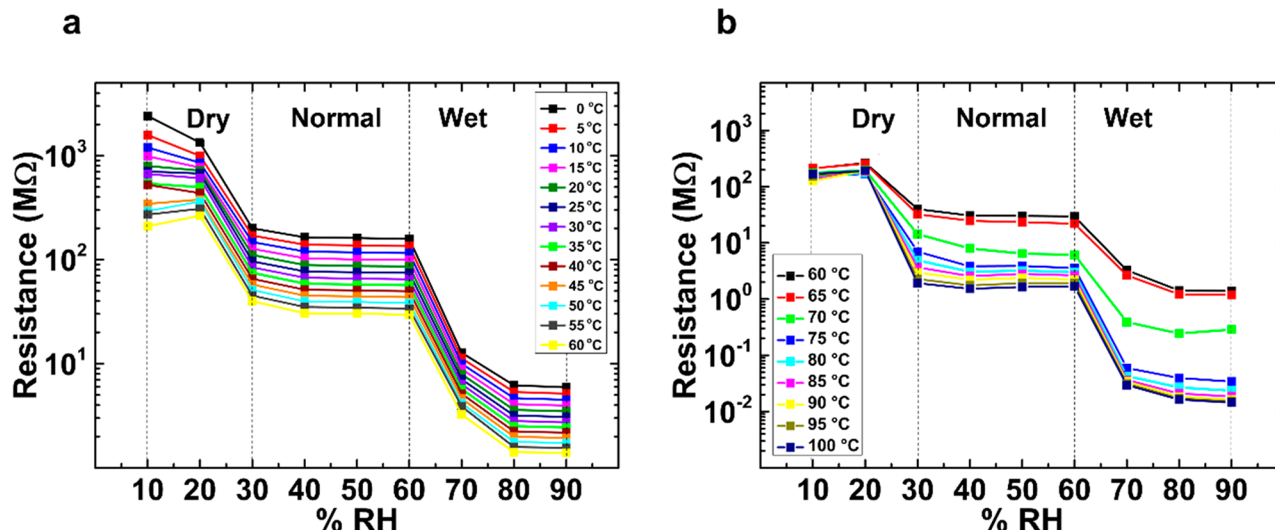


Figure 2. Thermal sensing response under different humidity conditions. (a) Resistance vs %RH from 0 to 62 °C. (b) Resistance vs %RH from 62 to 100 °C.

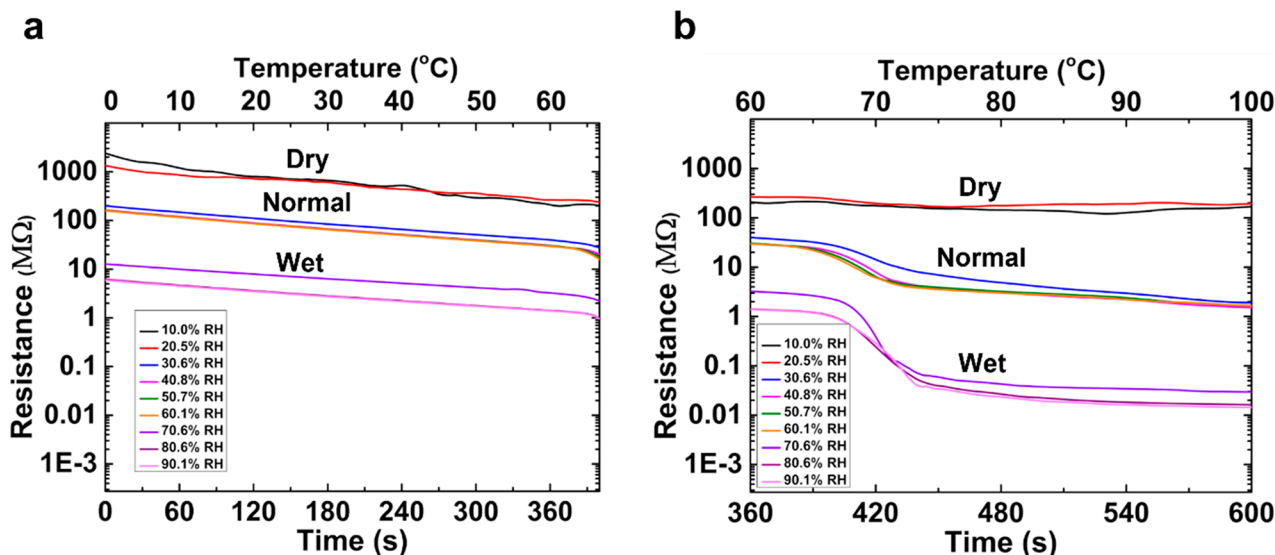


Figure 3. Thermal sensing response under different humidity conditions. (a) Resistance vs time for 0–62 °C at different %RH values. (b) Resistance vs time for 62–100 °C at different %RH values.

remotely monitored environmental temperature sensing applications. To the best of our knowledge, this work shows for the first time the application of a two-terminal VO₂-thin-film-based device as a thermal sensor, studied under the influence of varying humidity levels.

RESULTS AND DISCUSSION

We present two-terminal VO₂-thin-film-based devices for temperature sensing, as shown in Figure 1a. Around 150 nm film thickness with a patch size of 300 × 300 μm² of VO₂ was used as the sensing material. We choose Pt as the electrode due to its thermal and chemical stability.^{26–28} The width, *w*, and distance between electrodes, *d*, are 100 and 296 μm, respectively.

Characterization of VO₂ Thin Films. The stoichiometry of crystalline vanadium oxide is confirmed using X-ray photoelectron spectroscopy (XPS). Figure 1b shows the core-level spectra for vanadium (V 2p) and oxygen (O 1s). The fitted data shows V 2p_{3/2} peaks at 516.4 ± 0.2 eV

corresponding to V⁴⁺ and 517.5 ± 0.2 eV corresponding to V⁵⁺, thus confirming the functional oxide is composed of V⁴⁺ and V⁵⁺ components that correspond to VO₂ and V₂O₅, respectively. The V–O peak is resolved with the O 1s spectrum at 530 ± 0.2 eV. The core-level spectra of V 2p and O 1s presented here are identical to reported studies in the literature^{25,29,30} and are within the instrument error margin of ±0.2 eV. Another peak was observed at 532.3 ± 0.2 eV that corresponds to Si–O bonds from the substrate.³¹ The higher percentage of V⁴⁺ component (V⁴⁺ = 32.63%, V⁵⁺ = 18.96%, and V–O = 48.41%) confirms VO₂ (or V⁴⁺) as the major contributor in our mixed-phase vanadium oxide films.

X-ray diffraction (XRD) was performed on the post-deposition annealed VO₂ thin films on SiO₂/Si substrate, as shown in Figure 1c. The diffractogram of the crystalline films on SiO₂/Si confirms a (011) alignment at a 2θ value of ~27.2 corresponding to the monoclinic VO₂ (M1) phase.^{32,33}

Figure 1d shows the temperature-dependent Raman spectra of VO₂ thin films. The Raman peaks at 193 (A_g), 225 (A_g), 264

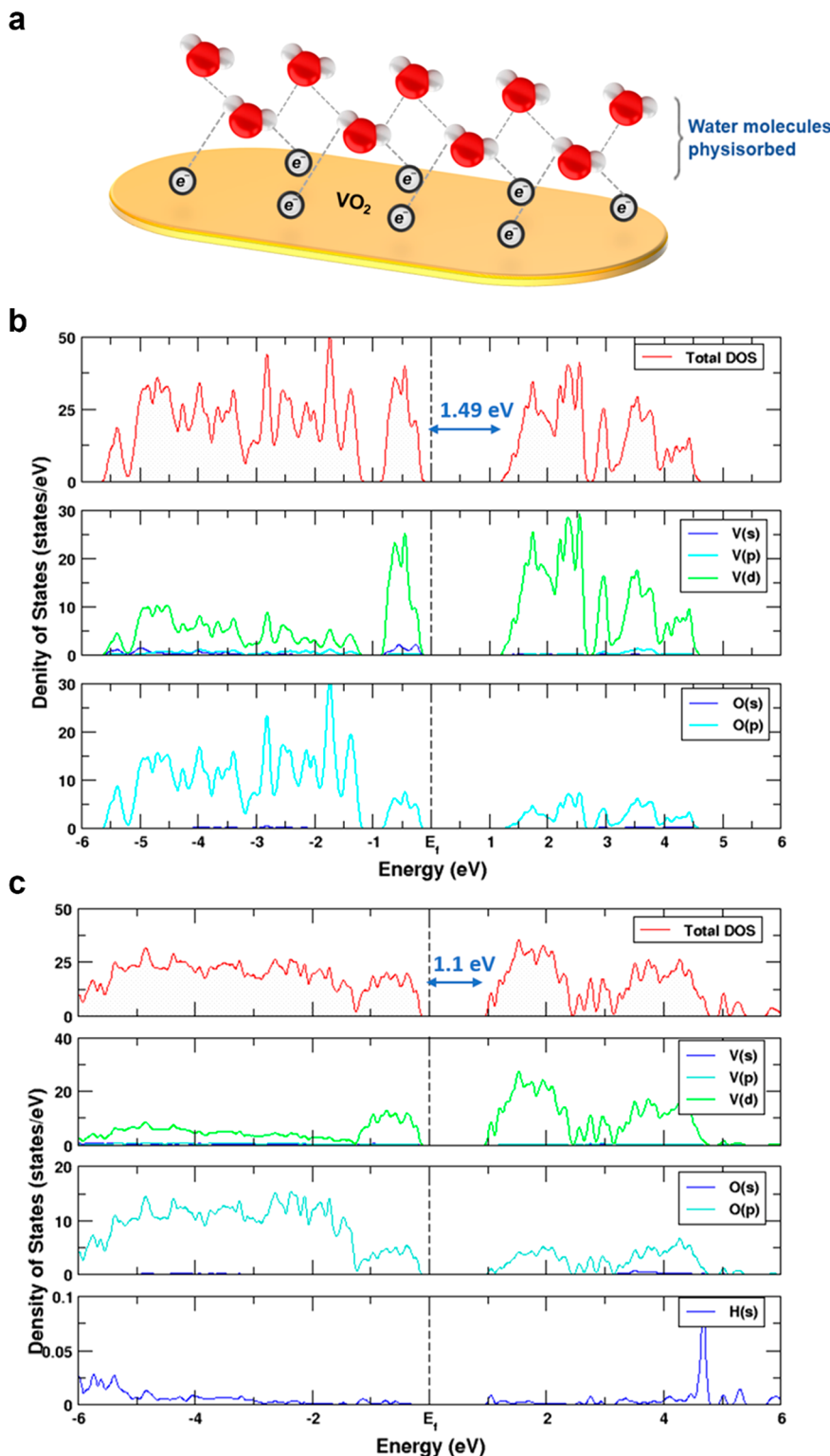


Figure 4. Density functional theory analysis of the reaction mechanism. (a) Schematic showing the mechanism of the thermal sensing response under humidity conditions. (b) The PDOS of the VO_2 pristine surface. (c) The PDOS of the VO_2 surface after adsorption of H_2O .

(B_g), 307 (A_g), 387 (A_g), 503 (A_g), and 612 (A_g) cm^{-1} confirm the presence of VO_2 (M1).^{25,34,35} The temperature-dependent Raman spectra show a reduction in peak intensity with increasing temperature, indicating an insulator (M1 phase) to metal (R phase) transition has taken place. It is also important to consider the impact of the Raman laser which induces

localized heating, which makes the film transition phase at 65 °C.

Effect of Humidity Levels on Thermal Sensing Response. The effect of varying humidity levels on the thermal sensing response of the VO_2 sensor was studied under three different humidity regions—dry, normal, and wet—in three different phases of the devices corresponding to the

insulator phase region, IMT slope region, and metallic phase regions, as shown in Figure 2 and Figure 3.

Region I: Insulator Phase Region (0–62 °C). VO₂ remains in the HR phase in this temperature region. Measurements were done from 10% relative humidity (RH) to 90% RH levels. It was observed, as seen in Figure 2a and Figure 3a, that dynamic temperature sensing had significant characteristic responses for three different humidity ranges: 10–20% RH (very dry), 30–60% RH (normal humidity range), and 70–90% RH (very wet) conditions. With increasing %RH levels, the resistance offered by the material decreases. On reaching 80% RH, there is a further drop in the resistance by an order of 10² for the same temperature. Under increased humidity, water molecules can be adsorbed through physisorption mechanisms.³⁶ For oxide-based humidity sensors that include zinc,³⁷ titanium,³⁸ and tin oxides,³⁹ a few mechanisms have been discussed in the literature. As %RH increases, the amount of water molecules that the VO₂ encounters also increases. In due course, as humidity levels increase to 80% RH and beyond, the VO₂ thin film accumulates several layers of water vapor percolating and sitting on its surface. The increased availability of water molecules increases the surface conductivity of the VO₂ film. This eventually causes a depletion of the VO₂ thin film layer, causing it to have lower resistance as a result of the increased surface conductivity of the VO₂ material.

Region II: Insulator-to-Metal Transition (IMT) Region (62–72 °C). *c*-VO₂ ideally remains in the insulator phase until 62 °C. Between 62 and 68 °C is the IMT slope region, wherein both insulator and metallic phases exist together. As observed from Figure 3, a similar trend is observed in terms of temperature sensing performance, wherein resistance drops for the same temperatures for increasing levels of humidity. The humidity levels also affect the phase transition temperature seen by a shift in the IMT region with increasing %RH, as shown in Figure 3b. With increasing %RH levels, it was observed that the IMT region shifts right, implying for increasing humidity levels that it takes a higher temperature for the material to transition from insulator to metallic phase region. A similar characteristic response has been observed where the threshold voltage was reduced exponentially when the %RH levels increased.⁴⁰ The humidity surrounding the VO₂ thin film leads to the adsorption of water molecules onto the surface. These water molecules are consequently dissociated into H⁺ and OH[−] as they percolate on the surface of the material. The H⁺ ions act as dopants, whereas the OH[−] ions percolate throughout the surface of the film.⁴¹ Increasing the H⁺ doping of VO₂ films leads to a decrease in the resistance. As humidity levels increase, there is increased percolation of OH[−] ions on the surface of the films.⁴² This slows down the doping of the VO₂ films with H⁺ ions, thus delaying the IMT phenomenon. Hence, a higher temperature is needed to initiate IMT as %RH levels increase. Another interesting observation was that under very dry conditions (humidity levels <30%RH) the IMT phenomenon was inhibited.

Region III: Metallic Phase Region (68–100 °C). At 68 °C, the device typically undergoes a transition from insulator to metallic phase. As observed in Figure 2b and Figure 3b, in the range from 62 to 100 °C, for a given temperature, resistance decreases with an increase in %RH. What is being observed is that, with increasing %RH for a fixed temperature, resistance decreases with an increase in %RH. Further, the

difference in resistance change from 62 to 100 °C is significantly high, wherein resistance drops by a factor of 10⁴ at 100 °C from 62 °C, as noted in Figure 2b. This is because, in the metallic phase region, resistance is lower than that of the insulator region. Owing to the polarity of the water molecules, at high humidity, these electrons are electrostatically attached to the positively charged hydrogen from the water molecules. These eventually form hydrogen bonds. This leads to a decrease in the density of free electrons on the surface of VO₂ film, thus leading to depletion of the VO₂ thin film layer and thereby lowering the resistance as a result of the increased surface conductivity of the VO₂ material. The rapid increase in surface conductivity in this region is due to the presence of abundant free electrons, as the material is now in the metallic phase. This leads to significant decreases in temperature-dependent resistance for increasing humidity levels, as observed in Figure 2b and Figure 3b. Further, characteristically distinct responses for the respective regions of very dry humidity conditions (10–20% RH), normal humidity conditions (30–60% RH), and very wet humidity conditions (70–90% RH) can be observed with notable resistance shift distinct to the three regions.

We can hereby understand that increasing humidity levels causes an increase in the IMT temperature, as the IMT region shifts toward the right with an increase in %RH levels. Also, there is a characteristic thermal response for each corresponding humidity level. Further, we are also able to clearly distinguish and categorize the thermal response of the sensor across the three different humidity regions—very dry, normal, and very wet conditions. Water vapor dissociates into H⁺ and OH[−] species. The resistance of the device decreases with an increase in %RH levels due to the fact that there are more available H⁺ ions donating electrons to the VO₂ surface. As the %RH further increases, it also causes an increase in the availability of OH[−] ions that cover the surface of the VO₂ film. This slows down the availability of electrons to the film surface. Following this, the IMT shifts right as it takes more time and an increased temperature to undergo IMT.

Density Functional Theory (DFT) Computational Studies. From our experimental investigation, we observed that all of the devices came back to their initial states upon humidity exposure and cyclic heating–cooling. This suggests that the dominant mechanism in our VO₂ devices is physical adsorption (physisorption). Hence, chemical adsorption has been ruled out and we have focused on only physisorption during DFT calculation, as illustrated in Figure 4. In order to understand the effect of humidity on VO₂ thin film, we have envisaged the water adsorption on the VO₂ surface using density-functional-theory (DFT)-based electronic structure calculations. We have determined the electronic structure property in terms of the projected density of states (PDOS) and optical absorption spectra of the pristine VO₂ surface and how they change upon adsorption of a water molecule (H₂O).

Figure 4a shows a schematic depicting the physisorption mechanism occurring under the effect of different levels of humidity. We have also calculated the changes in the PDOS and optical absorption spectra for the VO₂ surface under the influence of the dissociated hydroxyl ion (OH[−]) and atomic hydrogen (H⁺). From our theoretical investigations, we have observed a substantial band gap change in the water-adsorbed VO₂ surface in comparison to the pristine VO₂ surface. The PDOS of the systems involving a pristine VO₂ surface and a water-adsorbed VO₂ surface are depicted in parts b and c of

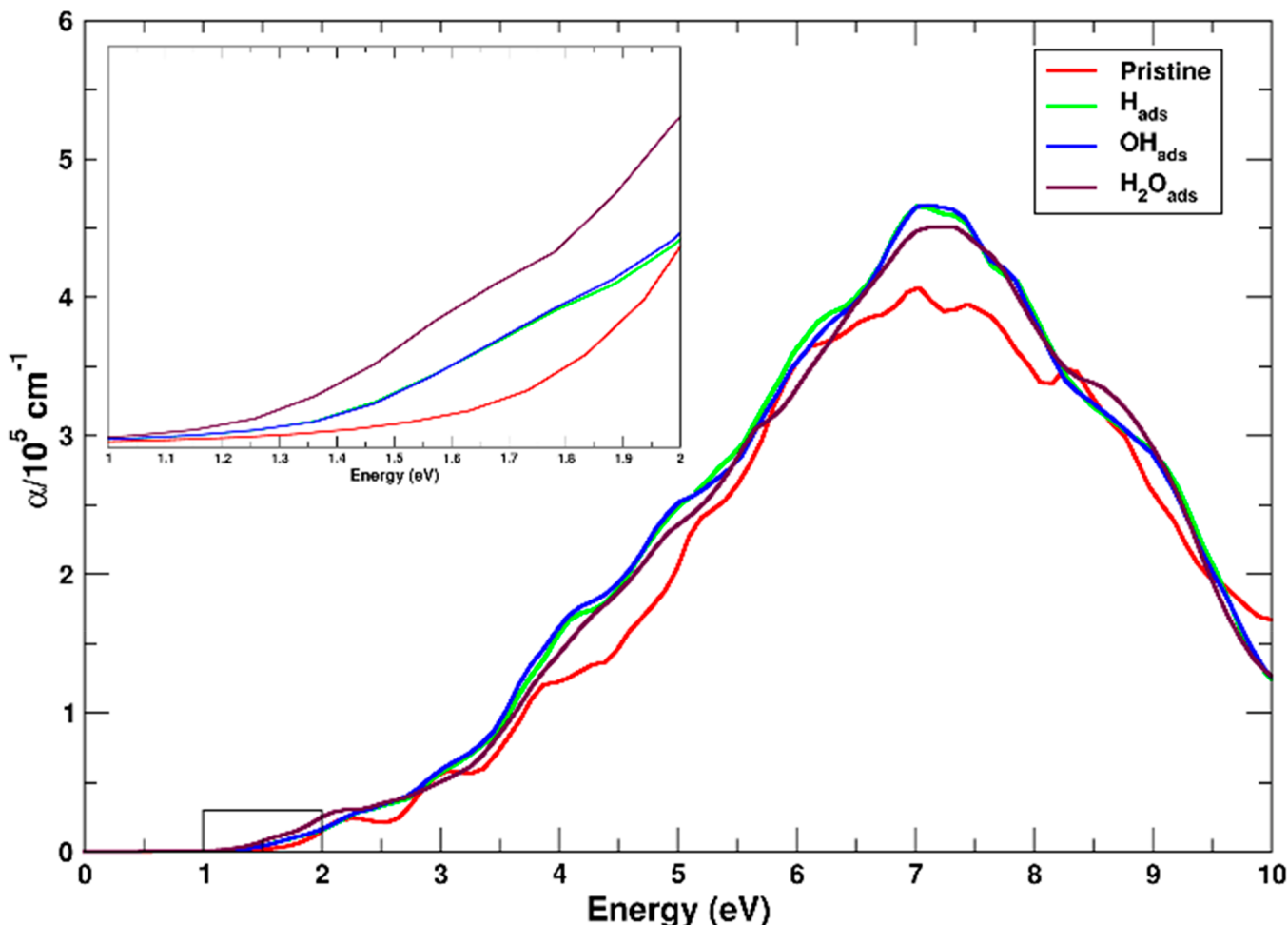


Figure 5. Comparison of optical absorption. Optical absorption spectra for the pristine VO_2 surface and after the adsorption of H^+ , OH^- , and H_2O .

Figure 4, respectively, to explore the corresponding band gap and the orbital contribution. The contribution for the valence band is predominantly from the outermost vanadium 3d orbital along with a minor contribution from oxygen 2p orbitals for both the pristine VO_2 surface and the water-absorbed VO_2 surface.

From the PDOS of the pristine VO_2 surface, the band gap is found to be 1.49 eV, as seen in Figure 4b. However, it can be observed from Figure 4c that after H_2O adsorption there is a clear decrease in the band gap from 1.49 to 1.1 eV and an increase in conductivity taking place, which is in good agreement with the experimental investigations—decreasing resistance with increasing humidity levels. Comparatively, significantly lesser changes in the band gap are observed during the adsorption of H^+ and OH^- ions on the VO_2 surface, as seen in Figure S1a and b. We have also calculated the optical absorption spectra which are shown in Figure 5. It can be seen from these spectra that the optical band gap is decreasing similarly to the electronic band gap on water molecule absorption. Our theoretical observation of substantial band gap change in the VO_2 surface upon water adsorption corresponds well with the experimental findings of the VO_2 sensing property being dependent on humidity levels.

Thermal Sensing Studies under Ambient Humidity Conditions. Temperature-dependent electrical characterizations were performed to understand the resistance-based temperature sensing performance of the as-fabricated VO_2

sensors. The device was found to exhibit thermal sensing response over a broad temperature range from -100 to 100 °C, as shown in Figure 6. With increasing temperature, the resistance was found to decrease. The sensor exhibits a linear

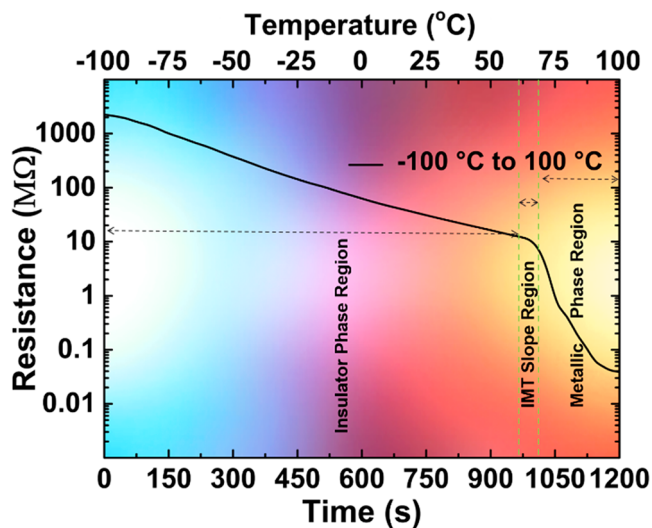


Figure 6. Temperature sensing measurements of the VO_2 thin film device. Resistance vs time for the temperature range from -100 to 100 °C under ambient humidity conditions.

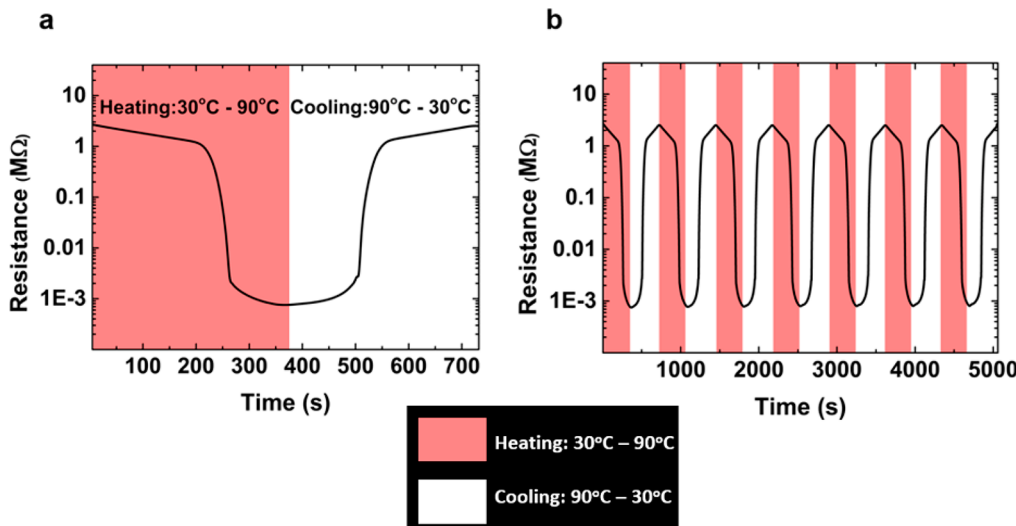


Figure 7. Temperature sensing measurements of the VO_2 thin film device. (a) Resistance vs time for the temperature range 30–90 °C for one cycle. (b) Resistance vs time measurements for the temperature range 30–90 °C for multiple heating–cooling cycles.

behavior starting from cryogenic temperatures through the freezing point (of water), 0 to 68 °C, from where the material transitions from the insulator phase to metallic phase region. This study was done under ambient lab humidity conditions with 51% relative humidity. Herein, we have studied the overall thermal sensing capabilities of the as-fabricated device under ambient conditions. The limitation encountered was that, below freezing temperature, the experimental setup was unable to effectively control humidity conditions within the LINKAM microenvironment due to rapid freezing of incoming water molecules. This can be seen in Figure S2. All temperature sensing measurements were taken by ramping the temperature at a rate of 10 °C/min and using a liquid nitrogen (LN_2) setup to accommodate the cooling ramp process.

Further, measurements were done within the sensor's response range for a temperature range from 30 to 90 °C. This particular range was selected to study and demonstrate desirable temperature sensing behavior owing to the limitation involving the volume of liquid nitrogen consumed by the system for the cooling cycles. A high volume of liquid nitrogen was required to perform cyclic performance testing, particularly below 30 °C. The volume of the LN_2 dewar used was 1 L, which was suitable to cover several cycles between the range of 30 and 90 °C. As seen from Figure 7a, with an increase in temperature, there is a decreasing trend in resistance in the heating cycle. Once it reaches 90 °C and the cooling cycle begins (decreasing temperature), the resistance starts increasing again. This is owing to the fact that VO_2 is a material that exhibits a negative temperature coefficient of resistance (NTC), hence showing a decrease in resistance with an increase in temperature. The sudden drop in resistance around 68 °C is due to the insulator-to-metal transition (IMT) phenomenon, which has been well discussed in the literature.^{43–46} The sharp decrease in the resistance hence corresponds to the transition of the VO_2 material from an insulator to a metal, thus denoting that the drastically lowered resistance is due to the material now being in the metallic phase region. Figure 7b shows the resistance change over five cycles of heating and cooling, which demonstrates the stability and repeatability of our VO_2 sensors. As observed from Figure 7a within the temperature range of 30–62 °C, the thermal

sensor operates in a HR state as the material is in the M1 insulator phase. After this, between 62 and 68 °C, is the IMT slope region, wherein both the metallic R phase and the insulator M1 phase coexist. From 68 °C onward, the material behaves in a LR state, as it is now completely in the metallic R phase.

It was found to have a TCR value of $-0.0243/\text{°C}$ in the temperature range from -100 to 62 °C which was found to be quantitatively much improved compared with previously reported values and for a broader range, as shown in Table 1. Cyclic repeatability of the sensor was exhibited, as shown in Figure 7b. The behavior observed in the temperature ranges shows that there is decreasing resistance with increasing temperature, which is in accordance with the NTC property of VO_2 material. The device sensitivity was $0.01 \text{ M}\Omega/\text{°C}$ between -100 and 62 °C, $1.03 \text{ M}\Omega/\text{°C}$ between 62 and 72 °C, and $0.031 \text{ M}\Omega/\text{°C}$ between 72 and 100 °C. We also found the sensor to have a response time of 0.83 s and a recovery time of 4.5 s, as shown in Figure S3 and Figure S4, respectively.

We can further understand that the various humidity levels do not affect the material property of our *c*- VO_2 thin film, as seen in the Raman spectra in Figure 8. The VO_2 thin film

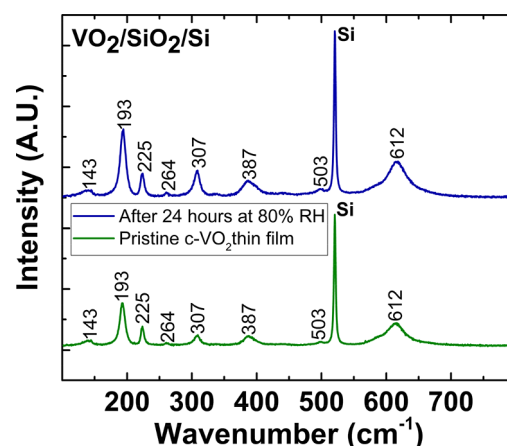


Figure 8. Raman spectra showing VO_2 (M1) peaks dominate both under pristine conditions and 24 h after exposure to 80% RH VO_2 .

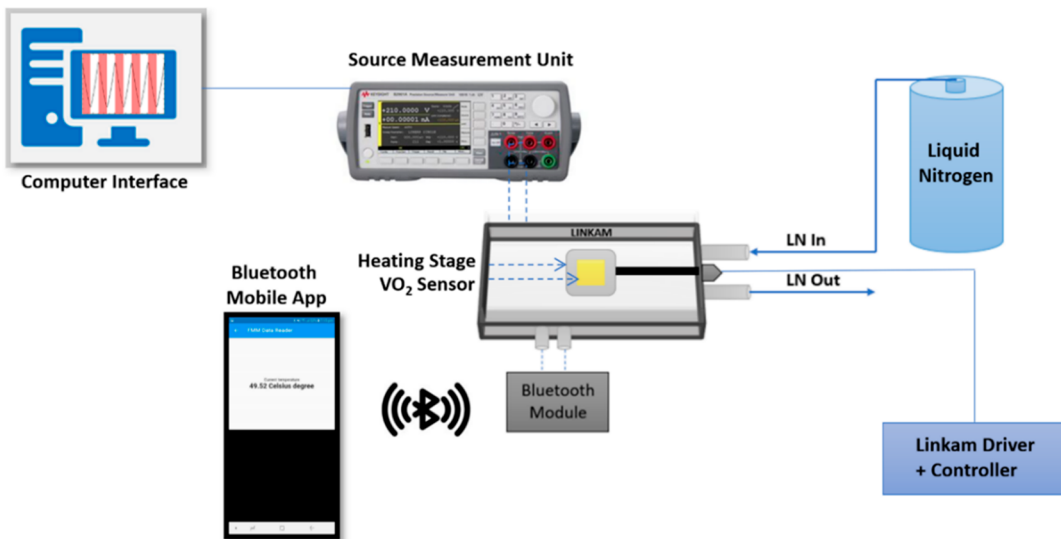


Figure 9. Schematic depicting the measurement setup including the Bluetooth module and the source measurement unit.

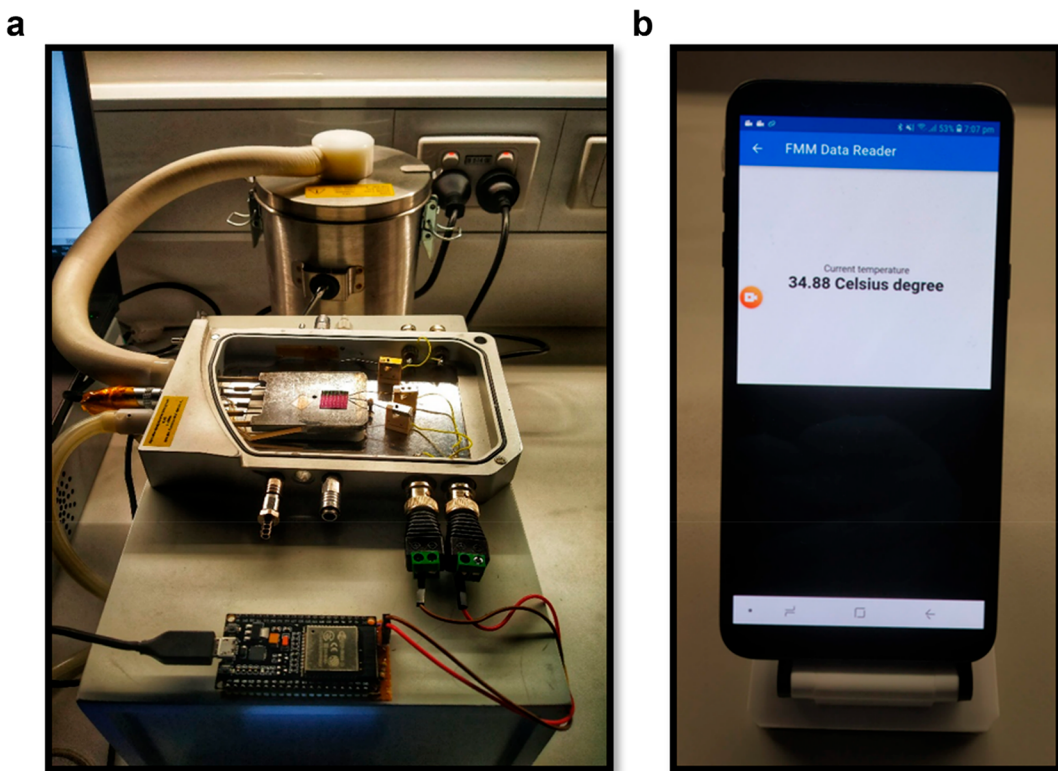


Figure 10. Wireless temperature sensor characterization. (a) VO_2 thermal sensor placed in the setup. (b) Temperature data being wirelessly read out using the BLE (Bluetooth low energy) module on data reader software.

remains in the M1 phase, as evidenced by the 193 (A_g), 225 (A_g), 264 (B_g), 307 (A_g), 387 (A_g), 503 (A_g), and 612 (A_g) cm^{-1} peaks corresponding to the M1 phase of VO_2 .^{25,34,35} There has been limited work reported on VO_2 -based thermal sensors until now, as shown in Table 1. In this work, we report a *c*- VO_2 -thin-film-based thermal sensing behavior under the effect of varying levels of humidity and study the underlying mechanism for the exhibited behavior. To the best of our knowledge, this is the first time the influence of humidity on thermal sensing behavior has been studied. All test bench

measurements were taken by employing a setup, as shown in the schematic in Figure 9.

Wireless Measurement Capabilities. Further, we demonstrated the wireless measurement capabilities of our fabricated VO_2 thin film temperature sensors. Figure 9 illustrates the schematic of the combined setup including the test bench measurement setup and Bluetooth module together. Simultaneously, measurements were done via both the test bench setup and displayed on the developed android application. Images depicted in Figure 10 show the VO_2 thermal sensor placed in the setup (Figure 10a) and the

dynamic temperature data being read on the FMM Data Reader (Figure 10b) under ambient humidity conditions of 51% RH. **Supplementary Video 1** shows the real-time display of the sensor's temperature sensing data on the Bluetooth application. The ESP32 module was chosen for achieving Bluetooth capabilities by interfacing it with the platinum electrodes on the VO₂ sensor device. Figure S5 shows the size perspective of a 7 × 7 array of devices held between two fingers. Figure S6 shows the miniaturized scale of an individual VO₂ thin film device and an array of 7 × 7 devices compared to the size of a \$1 (AUD) coin of diameter 28.65 mm. The miniaturized size of the device and the ability to achieve wireless measurement capabilities make this device a potential surface-mountable sensor that can be employed in exoskin and environmental sensing applications.

CONCLUSIONS

We have fabricated VO₂-based thermal sensors using DC sputtering and microfabrication techniques. The devices were investigated under the effect of humidity, wherein the thermal sensing response of the device was studied under varying levels of humidity conditions. It was found to have a characteristic thermal sensing response under very dry, normal, and very wet humidity conditions, thus showing a clear demarcation between the three classifications of humidity conditions. Given that VO₂ demonstrates three material phases, the devices also exhibited distinct thermal responses in these phases. In the metallic phase region, the device was found to have an individually independent thermal response for every humidity level from 10%RH to 90%RH. Also, the increase in humidity levels correspondingly caused a significant increase in the insulator-to-metal transition range temperatures. The overall effect of humidity on the thermal sensing behavior was such that, with increasing humidity levels, a corresponding decrease in the resistive thermal sensing response was exhibited. DFT-based calculations that were conducted showed that the experimental observations are closely correlated with the theoretical studies, thus clearly illustrating and hence substantiating that, with an increase in water molecule absorption, there is a decrease in resistivity offered by the VO₂ material. Further, wireless sensing capabilities have been demonstrated using the BLE module. This sensor could be used as a highly stable thermal sensor under humidity-dependent conditions. Such a sensor could find a wide range of applications from wearable surface-mounted environmental sensors to studying physical parameters in microclimates, such as plant wearables and precision agriculture monitoring. Future efforts may identify the effects of an insulation layer and packaging of the device on sensing response and properties.

MATERIALS AND METHODS

VO₂ Thin Film Deposition. Pulsed magnetron direct current (DC) sputtering was used to deposit approximately 150 nm thick VO₂ thin films on thermally grown silicon dioxide (300 nm) on silicon (SiO₂/Si) substrate. Sputtering of VO₂ was carried out using a vanadium metal target (99.999% pure) at room temperature in a 30% O₂ in Ar:O₂ gas mixture for 45 min. The pressure parameters were 4 mTorr and 4.8 × 10⁻⁷ Torr for sputtering and base pressure, respectively. The as-deposited VO₂ film was annealed using a standard air mixture in a tube vacuum furnace at 550 °C for 90 min. The annealing pressure was maintained at ~250 mTorr. Sputtering parameters for depositing VO₂ thin films using pulsed DC magnetron sputtering and film quality have been reported prior by Taha et al.³⁴

X-ray Photoelectron Spectroscopy. A Kratos AXIS Supra X-ray photoelectron spectrometer was used for collecting XPS data for post-annealed VO₂ thin film. Aluminum K-alpha X-rays with an excitation energy of 1486.7 eV are used as the radiation source. The spectra were collected under high vacuum pressure in constant analyzer energy (CAE) mode with a collection area of 110 μm². The core-level spectra were collected from a 300 × 300 μm² patterned crystalline VO₂ planar device deposited on SiO₂/Si substrate. For peak correction, adventitious carbon is taken as a reference at 284.8 eV. Peak fitting and analysis of VO₂ were performed using casaXPS software.

X-ray Diffraction. XRD studies were done by using an X-ray diffraction powder analyzer (D2 Phaser, Bruker) to investigate the crystallinity of post-deposited annealed VO₂ thin films. The peaks were detected using a monochromatic X-ray diffractometer with Cu Kα radiation (1.54 Å). The operating voltage and current were 40 kV and 40 mA, respectively. We scanned the samples in a range of 2θ from 20° to 40° with a scanning rate of 0.05°/min.

VO₂ Device Fabrication. A standard image reversal photolithography technique with a two-step lift-off process was used in the fabrication of the reported thermal sensor. The device was fabricated on a precleaned SiO₂/Si wafer. At first, metal electrodes were patterned using an AZ5214E photoresist. Following this, 25 nm of Pt on 5 nm of Ti was deposited using an electron beam evaporator system (Kurt J. Lesker PVD 75). Then, VO₂ film was sputtered using the Lesker PVD 75 Magnetron Sputterer system for a thickness of approximately 150 nm. Both steps were followed by a lift-off process. During the second lift-off process, DI water was avoided to prevent the washing-off of amorphous VO₂.^{47,48} Finally, the as-deposited VO₂ thin film was annealed in a vacuum furnace (VBF-1200X-MTI Corporation) at 550 °C for 90 min.

Electrical Testing. A model LTS420E-P Linkam stage was used for all electrical testing where samples were tested within the LINAKM chamber, including heating and cooling cycles. The liquid nitrogen canister was connected to the LTS420E-P stage to aid in cooling cycles of the experiment. A Linkam RH95 humidity controller setup was used to control the relative humidity within the Linkam stage microenvironment. The probes within the LTS420E-P used for all electrical testing were made of Au coated W tips. A Linkam T95 controller system with Linkpad was used to establish controlled settings for the heating and cooling cycles. B2901A was used to measure the device response, and Quick IV measurement software was used to control settings for the B2901A instrument and extract response data. The temperature was increased/decreased continuously, and the resistance changes were also continuously measured accordingly. The temperature was increased at a rate of 1 °C every 6 s. Raman spectra were collected using a Horiba Scientific LabRAM HR evolution Raman spectrometer facilitated with a 9 mW, 532 nm laser. The measurements were conducted using a 100× objective with a spatial resolution of ~321 nm and 1800 lines/mm grating.

Computational Methodology. We have performed first-principles calculations within the framework of the density functional theory (DFT) formalism to investigate the effect of adsorption of a water molecule on the VO₂ surface from the perspective of band gap change.⁴⁹ This will give us the understanding of moisture sensing by a VO₂-based sensor. We have employed Vienna Ab initio Simulation Package (VASP) code throughout the theoretical calculations, where the projector augmented wave (PAW) formalism has been implemented.^{50,51} The Perdew–Burke–Ernzerhof (PBE) form of the generalized gradient approximation (GGA) is used as the exchange-correlation functional, whereas a cutoff energy of 500 eV has been found to be well converged to carry out the subsequent ionic relaxation and geometry optimizations.⁵² We have constructed a 2 × 2 × 1 supercell containing 16 vanadium atoms and 32 oxygen atoms, and an adequate vacuum has been added in order to avoid the periodicity. The Brillouin zone is sampled using the 3 × 5 × 1 Monkhorst–Pack scheme for the VO₂ surface for the ionic relaxation.⁵³ The geometrical relaxations are carried out until ionic relaxation has obtained an energy cutoff of 10⁻³ eV and force convergence criteria of 10⁻² eV/Å. We have also studied the effect of

adsorption of O and OH molecules along with H₂O on the surface of VO₂. We have considered that these molecules are adsorbed at different positions like hollow, top, and bridge, different orientations, and different distances from the surface and obtained the minimum energy configuration of the optimized system for checking the adsorption characteristic as physisorption or chemisorption. We have also determined the optical absorption spectra for the pristine and adsorbed VO₂ surface in order to correlate the band gap variation upon the adsorption. Due to the presence of a d orbital in vanadium, we have used a Hubbard *U* parameter with a *U*_{eff} value of 3.4 eV for vanadium to have a better estimation of the band gap.⁵⁴

ASSOCIATED CONTENT

Supporting Information

The Supporting Information is available free of charge at <https://pubs.acs.org/doi/10.1021/acsaem.2c01110>.

Supplementary figures showing the PDOS of the VO₂ surface after H⁺ and OH⁻ adsorption, an image of the complete measurement setup, an image of the time constant extrapolation, an image of the recovery time extrapolation, a photo of the 7 × 7 array of VO₂ sensor devices fabricated on SiO₂ substrate, and an image displaying the miniaturized scale of an individual VO₂ thin film device and an array of 7 × 7 devices compared to the size of a \$1 (AUD) coin ([PDF](#))

Supplementary video showing the real-time display of the sensor's temperature sensing data on the Bluetooth application ([AVI](#))

AUTHOR INFORMATION

Corresponding Authors

Peter Francis Mathew Elango – *Functional Materials and Microsystems Research Group and the Micro Nano Research Facility, RMIT University, Melbourne 3001, Australia;* Email: peter.francis.mathew.elango@student.rmit.edu.au

Madhu Bhaskaran – *Functional Materials and Microsystems Research Group and the Micro Nano Research Facility, RMIT University, Melbourne 3001, Australia;* orcid.org/0000-0003-4319-1081; Email: madhu.bhaskaran@rmit.edu.au

Authors

Sumaiya Kabir – *Functional Materials and Microsystems Research Group and the Micro Nano Research Facility, RMIT University, Melbourne 3001, Australia; Department of Electrical and Electronic Engineering, Rajshahi University of Engineering & Technology, Rajshahi 6204, Bangladesh*

Ponnappa Kechanda Prasanna – *Materials Theory for Energy Scavenging (MATES) Lab, Harish-Chandra Research Institute (HRI), Allahabad 211019, India*

Mei Xian Low – *Functional Materials and Microsystems Research Group and the Micro Nano Research Facility, RMIT University, Melbourne 3001, Australia*

Mingie Yang – *Functional Materials and Microsystems Research Group and the Micro Nano Research Facility, RMIT University, Melbourne 3001, Australia*

Sudip Chakraborty – *Materials Theory for Energy Scavenging (MATES) Lab, Harish-Chandra Research Institute (HRI), Allahabad 211019, India;* orcid.org/0000-0002-6765-2084

Sumeet Walia – *Functional Materials and Microsystems Research Group and the Micro Nano Research Facility and School of Engineering, RMIT University, Melbourne 3001, Australia;* orcid.org/0000-0002-3645-9847

Sharath Sriram – *Functional Materials and Microsystems*

Research Group and the Micro Nano Research Facility, RMIT University, Melbourne 3001, Australia; orcid.org/0000-0002-8365-7504

Complete contact information is available at:

<https://pubs.acs.org/10.1021/acsaem.2c01110>

Notes

The authors declare no competing financial interest.

ACKNOWLEDGMENTS

Scholarship support from RMIT Research Stipend Scholarship (RRSS) and RMIT International Tuition Fee Scholarship is acknowledged. This work was performed in part at the Micro Nano Research Facility at RMIT University in the Victorian Node of the Australian National Fabrication Facility (ANFF). We acknowledge equipment funding from the Australian Research Council through LE150100001. Facilities and technical support from the RMIT Microscopy and Micro-analysis Facility, a node of Microscopy Australia, is acknowledged. P.K.P. and S.C. would like to acknowledge HRI Allahabad and DST-SERB Funding (SRG/2020/001707) for the infrastructure and funding. Computational work for this study was carried out at the cluster computing facility in the Harish-Chandra Research Institute (<http://www.hri.res.in/cluster>). We thank Paul Jones, Dr Chenglong Xu, and Dr Md. Ataur Rahman for helpful discussions and experimental support.

REFERENCES

- (1) Cui, Z.; Zhou, C.; Qiu, S.; Chen, Z.; Lin, J.; Zhao, J.; Ma, C.; Su, W. *Printed electronics: materials, technologies and applications*; John Wiley & Sons: 2016; pp 316–336.
- (2) Huang, C.-C.; Kao, Z.-K.; Liao, Y.-C. Flexible Miniaturized Nickel Oxide Thermistor Arrays via Inkjet Printing Technology. *ACS Appl. Mater. Interfaces* **2013**, *5* (24), 12954–12959.
- (3) Jin, Y. O.; John, D. S.; Podraza, N. J.; Jackson, T. N.; Horn, M. W. High temperature coefficient of resistance molybdenum oxide and nickel oxide thin films for microbolometer applications. *Optical Engineering* **2015**, *54* (3), 037101.
- (4) Azimi-Nam, S.; Golestan-Fard, F.; Hashemi, T. Formation of nickel-manganese oxide thermistors studied by XRD, SEM and auger spectroscopy. *J. Electron. Mater.* **1987**, *16* (2), 133–137.
- (5) Fau, P.; Bonino, J. P.; Demai, J. J.; Rousset, A. Thin films of nickel manganese oxide for NTC thermistor applications. *Appl. Surf. Sci.* **1993**, *65*–66, 319–324.
- (6) Gao, C.; Li, Z.; Yang, L.; Peng, D.; Zhang, H. Investigation of electrical and aging properties of Bi-modified (Zn_{0.4}Ni_{0.6})_{1-x}NaxO ceramic thermistors. *Journal of the European Ceramic Society* **2021**, *41* (7), 4160–4166.
- (7) He, Z.; Li, Z.; Xiang, Q.; Yan, W.; Zhang, H. Electrical properties of Y/Mg modified NiO simple oxides for negative temperature coefficient thermistors. *International Journal of Applied Ceramic Technology* **2019**, *16* (1), 160–169.
- (8) Dragoi, V.; Alexe, M. Cobalt-manganese oxide thin films thermistors obtained by MOD; 1998 International Semiconductor Conference. CAS'98 Proceedings (Cat. No. 98TH8351), October 6–10, 1998; pp 297–300, Vol. 1.
- (9) Syarif, D. G.; Ramelan, A. Electrical Characteristics of NTC Thermistor Ceramics Made of Mechanically Activated Fe₂O₃ Powder Derived from Yarosite. *AIP Conf. Proc.* **2008**, *989* (1), 122–125.
- (10) Dani Gustaman, S.; Engkir, S. Characterization of (Cuo-fe₂o₃) Ceramics with Three Different Compositions Sintered at 1100 Oc for Ntc Thermistor. *Indones. J. Mater. Sci.* **2007**, *8* (3), 272–276.

- (11) Li, P.; Zhang, H.; Gao, C.; Jiang, G.; Li, Z. Electrical property of Al/La/Cu modified ZnO-based negative temperature coefficient (NTC) ceramics with high ageing stability. *Journal of Materials Science: Materials in Electronics* **2019**, *30* (21), 19598–19608.
- (12) Yang, B.; Zhang, H.; Zhang, J.; Zhang, X.; Li, Z. Electrical properties and temperature sensitivity of B-substituted CuO-based ceramics for negative temperature coefficient thermistors. *Journal of Materials Science: Materials in Electronics* **2015**, *26* (12), 10151–10158.
- (13) Wegmann, M.; Brönnimann, R.; Clemens, F.; Graule, T. Barium titanate-based PTCR thermistor fibers: Processing and properties. *Sensors and Actuators A: Physical* **2007**, *135* (2), 394–404.
- (14) Rocha-Rangel, E.; Lopez Hernandez, J.; Rodriguez-Garcia, J. A.; Eddie Nahum, A.-M.; Calles-Arriaga, C. A.; Pech-Rodriguez, W. J.; Castillo-Robles, J. A. Dielectric properties of strontium titanate synthesized by means of solid state reactions activated mechanically. *Journal of Ceramic Processing Research* **2017**, *18*, 590–593.
- (15) Stenzel, C. Deployment of precise and robust sensors on board ISS-for scientific experiments and for operation of the station. *Anal. Bioanal. Chem.* **2016**, *408* (24), 6517–6536.
- (16) Cafuta, D.; Dodig, I.; Cesar, I.; Kramberger, T. Developing a Modern Greenhouse Scientific Research Facility-A Case Study. *Sensors (Basel, Switzerland)* **2021**, *21* (8), 2575.
- (17) Rusnick, M. R. Accurate temperature representation of storage conditions of human tissue and blood products: A cold chain analysis. *Int. J. Blood Transfus. Immunohematol* **2021**, *11*, 1.
- (18) Jha, A.; Tukkaraja, P. Monitoring and assessment of underground climatic conditions using sensors and GIS tools. *International Journal of Mining Science and Technology* **2020**, *30* (4), 495–499.
- (19) Urban, G.; Jachimowicz, A.; Kohl, F.; Kuttner, H.; Olcaytug, F.; Kamper, H.; Pittner, F.; Mann-Buxbaum, E.; Schalkhammer, T.; Prohaska, O.; Schönauer, M. High-resolution thin-film temperature sensor arrays for medical applications. *Sensors and Actuators A: Physical* **1990**, *22* (1), 650–654.
- (20) Baqir, M. A.; Choudhury, P. K.; Ibrahim, A. M. A. Metamaterial-Based Temperature Sensor Comprised of VO₂ Nano-Ribbons. *2019 16th International Conference on Electrical Engineering/Electronics, Computer, Telecommunications and Information Technology (ECTI-CON)*; 2019, pp 195–198.
- (21) Kim, B.-J.; Lee, Y. W.; Chae, B.-G.; Yun, S. J.; Oh, S.-Y.; Kim, H.-T.; Lim, Y.-S. Temperature dependence of the first-order metal-insulator transition in VO₂ and programmable critical temperature sensor. *Appl. Phys. Lett.* **2007**, *90* (2), No. 023515.
- (22) Liao, F.; Lu, C.; Yao, G.; Yan, Z.; Gao, M.; Pan, T.; Zhang, Y.; Feng, X.; Lin, Y. Ultrasensitive Flexible Temperature-Mechanical Dual-Parameter Sensor Based on Vanadium Dioxide Films. *IEEE Electron Device Lett.* **2017**, *38* (8), 1128–1131.
- (23) Junior, L. H. C. d. L.; Schelp, L. F.; Oliveira, L. C.; Neto, A. G. S. B.; Lima, A. M. N.; Neff, H. A fiber optical thermometer for high power transformer monitoring utilizing the thermo-optical phase transition of VO₂. *2012 IEEE International Instrumentation and Measurement Technology Conference Proceedings*; 2012, pp 1387–1390.
- (24) Karimov, K. S.; Mahroof-Tahir, M.; Saleem, M.; Chani, M. T. S.; Niaz, A. K. Temperature sensor based on composite film of vanadium complex (VO₂(3-fl)) and CNT. *Journal of Semiconductors* **2015**, *36* (7), No. 073004.
- (25) Kabir, S.; Nirantar, S.; Zhu, L.; Ton-That, C.; Jain, S. K.; Kayani, A. B. A.; Murdoch, B. J.; Sriram, S.; Walia, S.; Bhaskaran, M. Phase change vanadium dioxide light sensors. *Applied Materials Today* **2020**, *21*, 100833.
- (26) Haynes, W. M. *CRC Handbook of Chemistry and Physics*, 95th ed.; CRC Press: 2014.
- (27) Coursey, J. S.; Schwab, D. J.; Tsai, J. J.; Dragoset, R. A. *Atomic Weights and Isotopic Compositions (version 4.1)*; National Institute of Standards and Technology: Gaithersburg, MD, 2015; accessed November 2016.
- (28) Cottrell, T. L. *The Strengths of Chemical Bonds*; Butterworth: London, 1954; pp 71–101.
- (29) Hryha, E.; Rutqvist, E.; Nyborg, L. Stoichiometric vanadium oxides studied by XPS. *Surf. Interface Anal.* **2012**, *44* (8), 1022–1025.
- (30) Pergament, A.; Stefanovich, G.; Berezina, O.; Kirienko, D. Electrical conductivity of tungsten doped vanadium dioxide obtained by the sol–gel technique. *Thin Solid Films* **2013**, *531*, 572–576.
- (31) Aghaei, R.; Eshaghi, A. Optical and superhydrophilic properties of nanoporous silica-silica nanocomposite thin film. *J. Alloys Compd.* **2017**, *699*, 112–118.
- (32) Kabir, S.; Nirantar, S.; Monshipouri, M.; Low, M. X.; Walia, S.; Sriram, S.; Bhaskaran, M. Device Geometry Insights for Efficient Electrically Driven Insulator-to-Metal Transition in Vanadium Dioxide Thin-Films. *Advanced Electronic Materials* **2022**, *8* (1), 2100428.
- (33) Booth, J. M.; Drumm, D. W.; Casey, P. S.; Smith, J. S.; Seeber, A. J.; Bhargava, S. K.; Russo, S. P. Correlating the Energetics and Atomic Motions of the Metal-Insulator Transition of M1 Vanadium Dioxide. *Sci. Rep.* **2016**, *6* (1), 26391.
- (34) Taha, M.; Walia, S.; Ahmed, T.; Headland, D.; Withayachumnankul, W.; Sriram, S.; Bhaskaran, M. Insulator–metal transition in substrate-independent VO₂ thin film for phase-change devices. *Sci. Rep.* **2017**, *7* (1), 17899.
- (35) Zhang, S.; Chou, J. Y.; Lauhon, L. J. Direct Correlation of Structural Domain Formation with the Metal Insulator Transition in a VO₂ Nanobeam. *Nano Lett.* **2009**, *9* (12), 4527–4532.
- (36) Yin, H.; Yu, K.; Zhang, Z.; Zeng, M.; Lou, L.; Zhu, Z. Humidity Sensing Properties of Flower-Like VO₂(B) and VO₂(M) Nanostructures. *Electroanalysis* **2011**, *23* (7), 1752–1758.
- (37) Kulwicki, B. M. Humidity Sensors. *J. Am. Ceram. Soc.* **1991**, *74* (4), 697–708.
- (38) Schaub, R.; Thostrup, P.; Lopez, N.; Lægsgaard, E.; Stensgaard, I.; Nørskov, J. K.; Besenbacher, F. Oxygen Vacancies as Active Sites for Water Dissociation on Rutile TiO₂(110). *Phys. Rev. Lett.* **2001**, *87* (26), 266104.
- (39) Hahn, S. H.; Bârsan, N.; Weimar, U.; Ejakov, S. G.; Visser, J. H.; Soltis, R. E. CO sensing with SnO₂ thick film sensors: role of oxygen and water vapour. *Thin Solid Films* **2003**, *436* (1), 17–24.
- (40) Raja, V.; Hadiyal, K.; Nath, A. K.; Viannie, L. R.; Sonar, P.; Molina-Reyes, J.; Thamankar, R. Effect of controlled humidity on resistive switching of multilayer VO₂ devices. *Materials Science and Engineering: B* **2021**, *264*, 114968.
- (41) Yoon, H.; Choi, M.; Lim, T.-W.; Kwon, H.; Ihm, K.; Kim, J. K.; Choi, S.-Y.; Son, J. Reversible phase modulation and hydrogen storage in multivalent VO₂ epitaxial thin films. *Nat. Mater.* **2016**, *15* (10), 1113–1119.
- (42) Goodacre, D.; Blum, M.; Buechner, C.; Hoek, H.; Gericke, S. M.; Jovic, V.; Franklin, J. B.; Kittiwatanakul, S.; Söhnel, T.; Bluhm, H.; Smith, K. E. Water adsorption on vanadium oxide thin films in ambient relative humidity. *J. Chem. Phys.* **2020**, *152* (4), No. 044715.
- (43) Jepsen, P. U.; Fischer, B. M.; Thoman, A.; Helm, H.; Suh, J. Y.; Lopez, R.; Haglund, R. F. Metal-insulator phase transition in a VO₂ thin film observed with terahertz spectroscopy. *Phys. Rev. B* **2006**, *74* (20), 205103.
- (44) Hilton, D. J.; Prasankumar, R. P.; Fourmaux, S.; Cavalleri, A.; Brassard, D.; El Khakani, M. A.; Kieffer, J. C.; Taylor, A. J.; Averitt, R. D. Enhanced Photosusceptibility near T_c for the Light-Induced Insulator-to-Metal Phase Transition in Vanadium Dioxide. *Phys. Rev. Lett.* **2007**, *99* (22), 226401.
- (45) Nakajima, M.; Takubo, N.; Hiroi, Z.; Ueda, Y.; Suemoto, T. Photoinduced metallic state in VO₂ proved by the terahertz pump-probe spectroscopy. *Appl. Phys. Lett.* **2008**, *92* (1), No. 011907.
- (46) Zhan, H.; Astley, V.; Hvasta, M.; Deibel, J. A.; Mittleman, D. M.; Lim, Y.-S. The metal-insulator transition in VO₂ studied using terahertz apertureless near-field microscopy. *Appl. Phys. Lett.* **2007**, *91* (16), 162110.
- (47) Nirantar, S.; Mayes, E.; Rahman, M. A.; Ahmed, T.; Taha, M.; Bhaskaran, M.; Walia, S.; Sriram, S. In Situ Nanostructural Analysis of Volatile Threshold Switching and Non-Volatile Bipolar Resistive Switching in Mixed-Phased α-VO_x Asymmetric Crossbars. *Advanced Electronic Materials* **2019**, *5* (12), 1900605.

- (48) Nirantar, S.; Mayes, E.; Sriram, S. In Situ Transmission Electron Microscopy with Biasing and Fabrication of Asymmetric Crossbars Based on Mixed-Phased α -VO_x. *JoVE* **2020**, *159*, No. e61026.
- (49) Kohn, W.; Sham, L. J. Self-Consistent Equations Including Exchange and Correlation Effects. *Phys. Rev.* **1965**, *140* (4A), A1133–A1138.
- (50) Blöchl, P. E. Projector augmented-wave method. *Phys. Rev. B* **1994**, *50* (24), 17953–17979.
- (51) Kresse, G.; Furthmüller, J. Efficient iterative schemes for ab initio total-energy calculations using a plane-wave basis set. *Phys. Rev. B* **1996**, *54* (16), 11169–11186.
- (52) Perdew, J. P.; Burke, K.; Ernzerhof, M. Generalized Gradient Approximation Made Simple. *Phys. Rev. Lett.* **1996**, *77* (18), 3865–3868.
- (53) Monkhorst, H. J.; Pack, J. D. Special points for Brillouin-zone integrations. *Phys. Rev. B* **1976**, *13* (12), 5188–5192.
- (54) Stahl, B.; Bredow, T. Critical Assessment of the DFT + U Approach for the Prediction of Vanadium Dioxide Properties. *J. Comput. Chem.* **2020**, *41* (3), 258–265.

□ Recommended by ACS

Self-Powered Humidity Sensors Based on SnS₂ Nanosheets

Leyla Shooshtari, Raheleh Mohammadpour, *et al.*

NOVEMBER 07, 2022

ACS APPLIED NANO MATERIALS

READ

Methanol and Humidity Capacitive Sensors Based on Thin Films of MOF Nanoparticles

Miguel A. Andrés, Ignacio Gascón, *et al.*

JANUARY 07, 2020

ACS APPLIED MATERIALS & INTERFACES

READ

Piezoresistive Microcantilever with SAM-Modified ZnO-Nanorods@Silicon-Nanopillars for Room-Temperature Parts-per-Billion NO₂ Detection

Jiushuai Xu, Erwin Peiner, *et al.*

JUNE 05, 2020

ACS APPLIED NANO MATERIALS

READ

Sodium-Polyacrylate-Based Electrochemical Sensors for Highly Sensitive Detection of Gaseous Phenol at Room Temperature

Tea Romih, Samo B. Hočvar, *et al.*

JUNE 29, 2020

ACS SENSORS

READ

Get More Suggestions >